Fundamental insight into electrochemical oxidation of methane towards methanol on transition metal oxides

Aditya Prajapati[a,1] ⓘ, Brianna A. Collins[b,1] ⓘ, Jason D. Goodpaster[b,2] ⓘ, and Meenesh R. Singh[a,2] ⓘ

[a]Department of Chemical Engineering, University of Illinois at Chicago, Chicago, IL 60607; and [b]Department of Chemistry, University of Minnesota, Twin Cities, Minneapolis, MN 55455

Electrochemical oxidation of CH_4 is known to be inefficient in aqueous electrolytes. The lower activity of methane oxidation reaction (MOR) is primarily attributed to the dominant oxygen evolution reaction (OER) and the higher barrier for CH_4 activation on transition metal oxides (TMOs). However, a satisfactory explanation for the origins of such lower activity of MOR on TMOs, along with the enabling strategies to partially oxidize CH_4 to CH_3OH, have not been developed yet. We report here the activation of CH_4 is governed by a previously unrecognized consequence of electrostatic (or Madelung) potential of metal atom in TMOs. The measured binding energies of CH_4 on 12 different TMOs scale linearly with the Madelung potentials of the metal in the TMOs. The MOR active TMOs are the ones with higher CH_4 binding energy and lower Madelung potential. Out of 12 TMOs studied here, only TiO_2, IrO_2, PbO_2, and PtO_2 are active for MOR, where the stable active site is the O on top of the metal in TMOs. The reaction pathway for MOR proceeds primarily through $*CH_x$ intermediates at lower potentials and through $*CH_3OH$ intermediates at higher potentials. The key MOR intermediate $*CH_3OH$ is identified on TiO_2 under operando conditions at higher potential using transient open-circuit potential measurement. To minimize the overoxidation of $*CH_3OH$, a bimetallic Cu_2O_3 on TiO_2 catalysts is developed, in which Cu reduces the barrier for the reaction of $*CH_3$ and $*OH$ and facilitates the desorption of $*CH_3OH$. The highest faradaic efficiency of 6% is obtained using Cu-Ti bimetallic TMO.

electrochemical oxidation of methane | binding energy measurement | transient open-circuit potential | density functional theory | methanol synthesis

Electrochemical oxidation of methane (CH_4) at ambient conditions offers a sustainable route for efficient utilization of abundant natural resources, such as shale gas and biogas. However, the lower activity and selectivity of current electrocatalysts pose hurdles for the large-scale deployment of electrochemical technologies for efficient utilization of CH_4 (1). Currently, the majority (~66%) of CH_4-rich resources are burned to produce electricity or to provide heating for the residential and commercial buildings, which contributes ~1 gigaton of CO_2 emissions annually. CH_4 is also utilized to produce oxygenated chemicals such as CH_3OH using industrial processes like steam reforming followed by gas-phase conversion or direct thermocatalytic conversion (2). While the thermocatalytic routes often require high temperature and pressure and suffer from catalyst poisoning (3–5), the electrochemical technologies offer environmentally benign and sustainable routes for storing electrical energy by converting CH_4 and H_2O to CH_3OH and for generating electrical energy using a direct CH_4 fuel cell that primarily generates CO_2 (4, 6, 7). However, the primary challenge in such electrochemical processes is the first step of CH_4 activation on electrocatalysts, which is difficult at ambient conditions owing to its high C–H bond energy of 439 kJ/mol (8), high symmetry with tetrahedral molecular geometry, low polarizability of 2.448 $Å^3$ (9), the low solubility of 1.272 mM in the water at standard temperature and pressure (10), and competitive oxygen evolution reaction (OER) (11, 12). A complete understanding of the mechanism of electrochemical activation followed by oxidation of CH_4 and its competition with OER on transition metal oxides (TMOs) has not been developed yet. Consequently, there is a need for the experimental and theoretical evaluation of the activity and selectivity of methane oxidation reaction (MOR) on various TMOs to elucidate the origins of higher activation energy and competitive kinetics of MOR and OER and to identify strategies for selective synthesis of CH_3OH under ambient conditions.

There are very few experimental reports available on the kinetics of electrochemical MOR at ambient conditions (13). The majority of the MOR work focuses on the high-temperature electrocatalysis in galvanic cell configuration, such as solid oxide fuel cells (SOFCs), in which the primary objective is to harvest electrical energy by fully oxidizing CH_4 to CO_2 (14–18). The conventional SOFCs operating at a temperature range of 300 to 700 °C (17, 19) using Ni-based composite anode (20–22) have also been studied for partial oxidation of CH_4 to hydrocarbons (e.g., CO, C_3H_4, C_2H_6, and CH_3OH), but their operating efficiencies drop rapidly because of carbon deposition (coking) (6, 19, 23). The low-temperature electrolytic systems operating at temperatures <120 °C using Pt, Platinized-Pt, or Pt/Au catalysts have also been reported for partial oxidation of CH_4 to CH_3OH, but the faradaic efficiencies (FE) are too low for a practical purpose (11, 24–26). A comprehensive table of the current density, FE, and reaction products for MOR on various electrocatalysts along with electrolyte composition, temperature,

---

Significance

The electrochemical conversion of CH_4 to liquid fuel such as CH_3OH offers a sustainable and environmentally benign route to utilize shale gas. This process requires controlled oxidation by optimal splitting and formation of C–H and C–O bonds to produce desired products at ambient conditions, which has been a long-standing challenge in electrocatalysis of hydrocarbons. Here, we combine electrochemical experiments with quantum chemical calculations to develop activity descriptors for identification of efficient electrocatalysts that can partially oxidize CH_4 to CH_3OH. This work provides much deeper insights into potential-driven breakage/formation of C–H and C–O bonds, which will greatly advance the scientific understanding of hydrocarbon electrochemistry.

---

www.manaraa.com

and operating potential are provided in *SI Appendix*, Table S1. So far, only precious metals like Pt, Pd, Ru, and Au have been explored for MOR either under harsh chemical conditions or at very high overpotentials (11, 27–29). Further experimental evaluation of activity, selectivity, and mechanism of MOR over other transition metal catalysts is required to identify efficient MOR catalyst and uncover fundamental limits of CH_4 activation on these catalytic systems. It is also desirable to develop a theoretical understanding of the competitive mechanism of MOR and OER on these TMOs and identify the noncompetitive routes for partial oxidation of CH_4.

Theoretical investigations of CH_4 adsorption via C–H bond activation followed by electrochemical oxidation are necessary to identify the activity descriptors and fundamental scaling relationships for MOR on TMOs (30). CH_4, being a stable, nonpolar molecule, is known to bind weakly on the transition metals through a dissociative mechanism (31), whereas all the CH_x ($x = $ 1, 2, and 3) intermediates bind more strongly. Psofogiannakis and coworkers (32) showed that CH_4 oxidation to CO is preferable through the dissociative chemisorption of CH_4 on Pt with the sequence $*CH_3 \rightarrow *CH_2 \rightarrow *CH \rightarrow *CHOH \rightarrow *CHO \rightarrow *CO$. A similar study showed, depending on the surface structure, the oxygen-assisted dehydrogenation drives the selectivity of the reaction to either CH_xO_y or CO_x products (33). The presence of oxygen on transition metals in the form of metal oxides has been determined to play a key role in C–H bond activation and the oxidation of CH_4 (34–36). Under the anodic overpotentials, the dissolved CH_4 dissociates to form $*O$–CH_3 (CH_3 bonded to metal oxide) and $*O$–H. Because of H–C–H bond symmetry in CH_4 and CH_3, the energy needed to break (or activate) the C–H bond is equal to the energy required to transfer H from CH_4 to $*O$ (metal oxide). Therefore, the suggested activity descriptor for MOR is E_{OH}–E_O, whereas the activity descriptor for OER based on the rate-limiting step ($*OH \rightarrow *O$) is E_O–E_{OH} (37–40). The participation of $*O$ species in both MOR and OER is the primary cause for the competitive kinetics determining the selectivity of CH_4 oxidation on TMOs.

Regardless of the catalyst structure and composition, there has been an agreement in acknowledging that MOR proceeds through a dissociative mechanism. However, in the oxidation regime of the electrocatalytic MOR, the metals exist in the form of their oxides, and one descriptor (either E_H or E_{OH}–E_O) may not be sufficient to identify efficient catalyst, as the MOR activity can also depend on the binding energy of the CH_x to the metal oxide surface, and the availability of metal oxide sites to bind with CH_x and consequently to suppress OER (40, 41). Rossmeisl and coworkers (40) elucidate this further by studying the limitations of CH_3OH production on different TMO (110) surfaces. They show that activation energy for MOR is correlated with the reactivity of an adsorbed oxygen atom from the electrolyte. A catalyst is providing more reactive oxygen results in low energy barriers for OER, which leads to the suppression of MOR. Here, we hypothesize that the higher MOR activity requires higher values of E_{OH}–E_O, the higher surface coverage of $*O$ and a noncompetitive binding site of $*O$. Hence, studying the activity descriptors in combination with the estimation of the binding energy of the CH_x species, the surface coverage of oxygen ad-atoms, and the availability of competitive versus noncompetitive sites for CH_x adsorption on TMOs are expected to provide mechanistic insights to identify active electrocatalysts.

In this article, we recognize the experimental challenges associated with C–H bond activation and mass transfer limitations of CH_4 in aqueous electrolytes as well as theoretical shortcomings because of a lack of comprehensive information about the MOR mechanism over TMOs. To address these challenges, we conduct controlled electrochemical experiments to study the activity and selectivity of CH_4 oxidation over 12 TMOs, Sc_2O_3, TiO_2, ZrO_2, Fe_2O_3, Co_3O_4, IrO_2, NiO, PtO_2, Cu_2O_3, ZnO, SnO_2, and PbO_2, in

near-neutral and alkaline electrolyte using rotating-disk electrode cell, followed by theoretical evaluation of efficient MOR catalysts using density functional theory (DFT). To elucidate the mechanism of MOR, we implement experimental studies to measure the binding energy of CH_4 using reactant–impulse chronoamperometry (RIC), detect key reaction intermediate CH_3OH using transient open-circuit potential (t-OCP) measurement, and measure reactions product using chromatography.

The objectives of this study are to relate the activity of MOR to the binding energy of CH_4, identify the noncompetitive active sites for MOR-active catalysts, and determine reaction pathways and strategies to direct partial oxidation of CH_4 to CH_3OH. The remainder of the article is organized as follows. *Methods* explains the DFT calculations to estimate the adsorption energies and activation barriers of MOR and OER on TMO surfaces. *Experimental Materials and Methods* describes the setup of the electrochemical cell, preparation of the electrodes, the binding energy estimation, product distribution, and t-OCP experiments. *Results and Discussion* presents FE for the active TMOs, optimal binding energy range for MOR estimated by experimental methods, reaction profiles of MOR and OER on TMO surfaces showing relative energies of the adsorbed intermediates by computational methods, a discussion on favorable reaction pathways for MOR by combining both experimental and computational methods, and a strategy to produce CH_3OH using CuTi bimetallic catalyst. *Conclusions and Perspectives* presents conclusions and prospects in choosing/synthesizing efficient electrocatalysts for CH_4 oxidation.

Methods

DFT Calculations to Estimate Binding Energies and Free Energy Profile. Estimated energies of adsorption and the free energy profile on four metal oxide surfaces, IrO_2, PbO_2, TiO_2, and SnO_2, have been calculated with DFT Vienna Ab initio Simulation Package (VASP) 5.3.5 (42). Calculations were performed using the Perdew-Burke-Ernzerhof (PBE) exchange-correlation functional with Grimme's D3 corrections (43, 44). Here, the metal oxide (110) surfaces were modeled using a four-layer (4×4) periodic slab, and the successive slabs were separated by at least 25 Å of vacuum. Adsorption was allowed only on one side of the slab. Partial occupancies for each orbital were populated using the Fermi smearing method with a width of 0.1 eV. All energies reported were sampled at a $4 \times 4 \times 1$ Monkhorst–Pack k-points and a 350 eV planewave cutoff. The convergence of total energy for the planewave cutoff and the k-point set are summarized in *SI Appendix*, section S. 13. The computational hydrogen electrode model was used to calculate the energy of reaction intermediates, and an applied potential of 2.11 V versus reversible hydrogen electrode (RHE) is applied in all energy calculations (45). Solvation effects were modeled by reporting all energies with the corrections gained from the implicit solvation model, VASPsol (46).

Experimental Materials and Methods.

Electrochemical product distribution. Transition metal plates of Sc, Ti, Fe, Co, Ni, Cu, Zn, Zr, Ir, Pt, Sn, and Pb (>99.9% purity, ACI Alloys) of 1-mm thickness were cut into disks of 8-mm diameter and polished using alumina suspensions followed by sonication in deionized water and drying under Ar flow. The Cu–Ti bimetallic catalyst was prepared by electrodepositing Cu on Ti disk from 0.1 M Cu (NO_3)$_2$ (pH = 2) at −2 V versus Ag/AgCl for 45 min. The disk was finally weighed to determine ~10% loading of Cu on Ti. Electrochemical experiments were performed in a custom, three-dimensionally printed, two-compartment H-Cell separated by an anion exchange membrane (Excellion, SnowPure technologies) with the transition metal disks as the working electrodes, Ag/AgCl microreference electrode (Innovative Instruments), Pt strip as the counter electrode, and ~6 mL of a well-stirred 0.1 M phosphate buffer solution (pH 7.0) or 0.1 M KOH (pH 13.0). Linear sweep voltammetry was performed under oxidation potentials to develop an oxide layer, which was followed by chronoamperometry in a CH_4-sparged H-Cell for ~2 h at potentials in the range of 1.5 to 2.4 V versus RHE. At the interval of 20 min, the gas products evolved were detected by passing the outlet from the H-Cell to an SRI GC 8610C MG#5 to quantify gaseous products. A detailed experimental setup and the experimental procedure can be seen in *SI Appendix*, section S.2.

Characterization of electrodes. The metal oxide electrodes for MOR were characterized by scanning electron microscopy (SEM), energy dispersive X-ray spectroscopy (EDS), and X-ray photoelectron spectroscopy (XPS) before and after electrocatalysis. SEM and EDS were performed using Hitachi S4800 Field

Emission SEM. XPS measurement was conducted using Thermo Scientific ESCALAB 250XI microprobe with an Al Kα source. Details of characterization can be found in *SI Appendix*, section S.5.

Reactant-impulse chronoamperometry for estimation of CH₄ binding energy. The dissolved CH₄ in the electrolyte must bind or at least interact with the active sites on the electrode before the activation of the C–H bond can occur (47). It has been postulated that the activation of the C–H bond involves the dissociation of CH₄ to form *O–CH₃ and *O–H (40). The energy of such dissociative adsorption of CH₄ is difficult to measure. However, the binding energy of CH₄ in the preactivation step (* + CH₄ → *CH₄) can be measured and correlated with the CH₄ activation energy. Here, we perform an RIC in a rotating disk electrode (RDE) cell by switching the Ar-saturated electrolyte with the CH₄-saturated electrolyte at a potential lower than the onset potential for MOR (e.g., 1.52 V versus RHE). The Ar-saturated and CH₄-saturated electrolytes were prepared by presaturating respective gases in a 0.1 M potassium phosphate buffer at pH 7. The dynamic variation in the OER current density was measured by sequentially varying electrolyte feed in the following manner: first feeding Ar-saturated electrolyte for 10 to 15 min, followed by CH₄-saturated electrolyte for 10 to 15 min, and then back to Ar-saturated electrolyte. In general, the CH₄-saturated electrolyte was found to suppress the OER current density, which could occur by either direct binding of CH₄ to the free active sites (*) or binding of CH₄ to the O atom of OER intermediates (*OH, *O, *OOH, and *O₂). Therefore, the fractional coverage of *CH₄ can be estimated by calculating the change in the OER current density as described below (see *SI Appendix* for details):

$$\theta = \frac{I_{OER,Ar} - I_{OER,CH_4}}{I_{OER,Ar}},$$ [1]

where θ is the fractional coverage of the *CH₄ on the electrode surface, $I_{OER,Ar}$ is the OER current density in Ar-saturated electrolyte, and I_{OER,CH_4} is the OER current density in CH₄-saturated electrolyte. The equilibrium constant K for the CH₄ adsorption/desorption

$$CH_4 + {}^* \rightleftharpoons {}^*CH_4$$
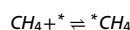
can be obtained from the Everett isotherm equation for a dissolved CH₄ in contact with a TMO surface (48).

$$K = \frac{\theta(1-x^*)}{x^*(1-\theta)},$$ [2]

where x^* is the mole fraction of dissolved CH₄ in the electrolyte. The binding energy can be estimated from the Gibbs free energy relation

$$\Delta G = RT \ln(K),$$ [3]

where R is the universal gas constant (8.314 J mol⁻¹K⁻¹)and T(298.15 K) is the temperature at which the experiments were performed.

t-OCP measurement for CH₃OH detection. The OCP identifies a mixed potential (or corrosion potential) when the multiple redox reactions—OER and MOR—are in equilibrium at net zero currents. The variation in OCP can be related to the variation in the activity of reactants and products in the double layer. Here, we use t-OCP measurement as a means to identify key reaction intermediates of MOR. The first step in t-OCP measurement is to perform chronopotentiometry to obtain a steady potential and FE at the desired current, which ensures fractional coverages of reaction intermediates also attain a steady state. The next step is to shift the applied current to zero and record t-OCP as the reaction intermediates go back from dynamic to static equilibrium. The t-OCP graph is sensitive to reaction pathways and coverages of stable reaction intermediates.

The t-OCP values for OER in Ar-saturated 0.1 M phosphate buffer were measured for initial currents of 0.25 mA and 0.5 mA in a custom-built H-cell with TiO₂ on RDE. The steady-state values of t-OCP were compared for 0.25 mA and 0.5 mA to verify the current-independent behavior of steady-state OCP for OER. Next, the t-OCP values for MOR were measured for an initial current of 0.25 mA (at 1.8 V versus RHE) and 0.5 mA (at 2.1 V versus RHE) on TiO₂ in a CH₄-saturated 0.1 M phosphate buffer solution. Since CH₃OH is one of the possible intermediates of MOR (32, 36), the variation in the fractional coverage of *CH₃OH will have a direct effect on the steady-state values of t-OCP. To identify the formation of *CH₃OH on TiO₂, a calibration curve was prepared by measuring the change in the steady-state values of t-OCP for increasing CH₃OH concentrations from 0 to 10 mM, which was added manually to CH₄-saturated 0.1 M phosphate buffer solution. This calibration curve was used to identify *CH₃OH produced at a higher current—0.5 mA. The detailed experimental setup and the experimental procedure can be seen in *SI Appendix*, section S.2.

Results and Discussion

Product Distribution and Faradaic Efficiency of CH₄ Oxidation in Near-Neutral and Alkaline Electrolytes.
Fig. 1 shows the product distribution obtained from the oxidation of CH₄-saturated electrolyte using the 12 stable TMO electrodes in neutral (pH 7.2) and alkaline (pH 13) conditions. The missing first-row transition metals such as V, Cr, and Mn in Fig. 1 were not stable in a wide pH range. The linear sweep voltammograms of all catalysts are shown in *SI Appendix*, section S.6. The product distributions under acidic conditions were also not investigated, as most TMOs dissolve in the oxidation regime, which can be seen from their Pourbaix diagrams in *SI Appendix*, section S.4. While O₂ is the dominant product on the majority of TMOs, CO₂ is produced only on TiO₂, IrO₂, and PbO₂ in phosphate buffer solution. Since phosphate ions can specifically adsorb and poison Pt surfaces (49, 50), PtO₂ did not show any activity toward MOR in phosphate buffer. However, a significant selectivity (∼10% FE) to MOR is observed on PtO₂ in 1 M KCl electrolyte. Comparing Fig. 1 *A* and *B*, it can be observed that these four active MOR catalysts show a higher FE in the neutral medium. This is because there is a higher concentration of OH⁻ in alkaline medium (0.1 M OH⁻) that specifically adsorbs to the positive electrode and oxidizes to produce O₂, which reduces the availability of the free site for MOR.

Fig. 2*A* shows the variation of FE of MOR producing CO₂ with increasing the applied potential of the active TMOs in the neutral pH phosphate buffer electrolyte. The onset potentials for
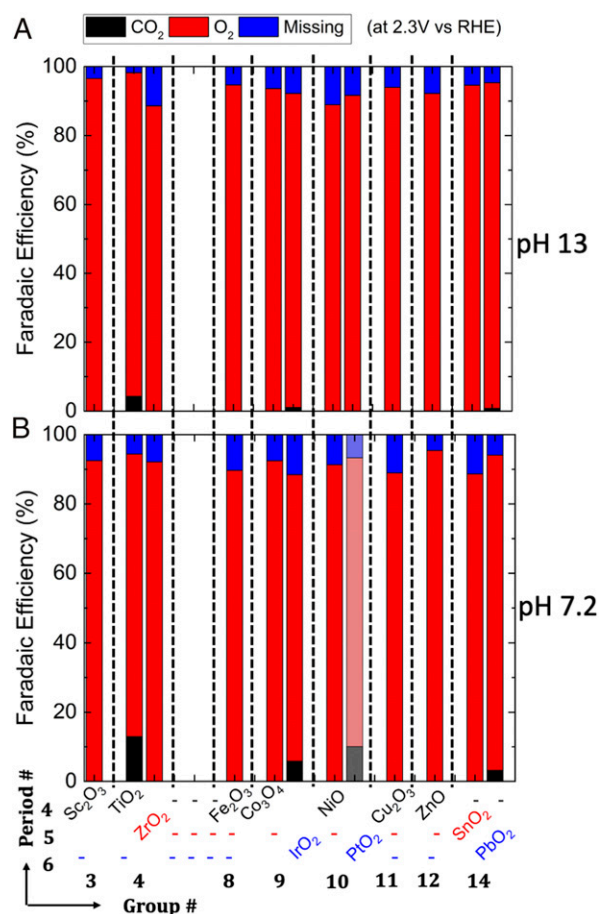
Fig. 1. Product distribution and FE of OER and MOR over stable TMOs in (*A*) 0.1 M KOH (pH = 13) and (*B*) 0.1 M potassium phosphate buffer (pH = 7). PtO₂ was found to be MOR inactive in 0.1 M potassium phosphate buffer. The shaded stacked bar for PtO₂ in *B* shows the FE and the product distribution using 1 M KCl (pH = 7).

Prajapati et al.
Fundamental insight into electrochemical oxidation of methane towards methanol on transition metal oxides

PNAS | 3 of 9
https://doi.org/10.1073/pnas.2023233118

www.manaraa.com

MOR are found to be 1.65, 1.9, and 2.1 V versus RHE for TiO_2, IrO_2, and PbO_2, respectively. These onset potentials are the lowest applied potentials for which the produced CO_2 was detected in GC. Fig. 2A also shows that TiO_2 has the highest FE of 13.5% at 2.31 V versus RHE. The decrease in FE of MOR at higher applied potential can be due to mass transfer limitations of dissolved CH_4. Fig. 2B shows the partial current densities of MOR producing CO_2 at different applied potentials. The Tafel slopes of MOR increase in the following order: PbO_2, 190 mV/dec; TiO_2, 232 mV/dec; and IrO_2, 274 mV/dec. The exchange current density also follows a similar trend: PbO_2, 6.5×10^{-13} mA/cm^{-2}; TiO_2, 9.2×10^{-11} mA/cm^{-2}; and IrO_2, 6.6×10^{-9} mA/cm^{-2}. IrO_2 has the highest intrinsic rate of MOR but suffers greatly from the higher Tafel slope. The larger Tafel slopes of these three TMOs are indicative of passive oxide layer formation, which increases the resistance for electron transfer (51).

Measurement of CH_4 Binding Energy on TMOs and Activity Descriptors for MOR. To further understand the origin of the MOR activity on IrO_2, TiO_2, PbO_2, and PtO_2, the binding energy of CH_4 on different TMOs are measured using RIC as described in *Experimental Materials and Methods*. Several experimental and theoretical works have reported that CH_4 adsorbs physically on the metal oxides, followed by the activation of the C–H bond (52–55). Here, we implement the RIC technique to measure the binding energy of CH_4 adsorption on TMOs in the potential range below the onset potential of CH_4 activation in MOR. In brief, the decrease in OER current density was measured by exchanging Ar-saturated electrolyte with CH_4-saturated electrolyte. The adsorption of CH_4 on TMOs decreases the active sites for OER and thereby decreases the OER current density, which can be used to estimate fractional


Fig. 2. (*A*) Faradaic efficiency and (*B*) partial current density of MOR producing CO_2 on TiO_2, IrO_2, and PbO_2 at different applied potentials in neutral pH phosphate buffer electrolyte.

coverage and binding energy of *CH_4 on TMOs. Fig. 3A shows the schematic of this reversible process of CH_4 binding to the TMO and its influence on OER intermediate coverages. Fig. 3B shows the effect of reversible adsorption/desorption on the OER current density on TiO_2 by cyclic feeding of Ar-saturated electrolyte followed by CH_4-saturated electrolyte at a fixed potential of 1.52 V versus RHE (which is less than onset potential of MOR). The relative change in the OER current density provides the fractional change in the coverage of *CH_4 (see Eq. **2**), which can be used in the Everett isotherm (Eq. **3** with Eq. **4**) to obtain the binding energy of *CH_4(E_{*CH_4}). Fig. 3C shows the binding energy of *CH_4 on 12 TMOs in near-neutral pH electrolyte at 1.52 V versus RHE. The measured binding energy of *CH_4 decreases with increasing the group number or decreasing the period number in the periodic table. A similar trend of adsorption energies of CH_4 on transition metals has been reported elsewhere (56, 57). It can be seen in Fig. 3C that the binding energies of CH_4 on MOR active catalysts—TiO_2, IrO_2, and PbO_2—are similar and in the range 0.24 ± 0.01 eV. PtO_2 is also a MOR active catalyst in neutral pH KCl electrolyte with the binding energy close to the optimal range. Also, the free energy change for the first step of MOR ($E_{*CH_4} - E_{*CH_3}$) for TiO_2, IrO_2, and PbO_2 is similar (Fig. 3C). Therefore, the binding energy of CH_4 can be considered as one of the activity descriptors for MOR, which governs only the surface coverage of *CH_4. The calculated surface coverages of *CH_4 on different TMOs are shown in *SI Appendix*, Fig. S3. The TMOs with the binding energy of CH_4 less than 0.23 eV are not active for MOR because of the lower surface coverages of *CH_4. However, there are a few catalysts such as Sc_2O_3, ZrO_2, and SnO_2 that have binding energies greater than 0.23 eV and are not active for MOR. This is due to competitive active sites for OER and MOR present on these catalysts (see *Competitive Pathways for OER and MOR on TMOs*).

The mechanism of CH_4 adsorption involves the transformation of tetrahedral (T_d) symmetry to the H–C–H bond-angle–distorted (D_{2d}) structure followed by C–H bond elongation and adoption to (C_s) conformation (47). These symmetry transformations can also be explained using the molecular orbital theory. The T_d symmetry of CH_4 (with bond angle 109.5°) has two occupied orbitals—a_1 and t_2—and two unoccupied antibonding orbitals—a_1^* and t_2^*. The interaction of CH_4 with TMO causes the threefold degenerate t_2 set to split into the destabilized b_2 state because of reduced overlap between 2p and 1s orbitals and the stabilized twofold degenerate e state because of an increase in C–H bonding character. Similarly, the unoccupied t_2^* orbital splits into a stabilized b_2^* state and destabilized a twofold degenerate e^* state because of the antibonding character of C–H bonds. The destabilization of t_2 and t_2^* orbitals results in the distortion of adsorbed CH_4 to attain D_{2d} conformation with an increased H–C–H bond angle of 120°. The formation of the distorted structure (D_{2d}) is then followed by the elongation of one of the C–H bonds to attain C_s conformation. The degree of C–H bond elongation governs the C–H bond activation on different TMOs. The schematics of molecular transformations during adsorption ($T_d \rightarrow D_{2d}$) of CH_4 followed by activation ($D_{2d} \rightarrow C_s$) are shown in *SI Appendix*, Fig. S12.

The interactions between CH_4 and TMO are mostly electrostatic in the nonfaradaic region of MOR. The coulombic interaction between TMO and CH_4 helps in the stabilization of b_2 state of t_2 orbital and thereby the adsorption of CH_4. Therefore, the electrostatic (or Madelung) potential of the metal in the TMO should have a direct effect on the measured binding energy of CH_4. Fig. 3D shows a nearly linear trend between the measured binding energy and the Madelung potential of metal in TMOs. The Madelung potentials for TMOs were obtained from ref. 58. The MOR active catalysts have lower Madelung potentials (< -40 V) as compared to the other inactive catalysts. It can be inferred from Fig. 3D that the MOR active catalysts should
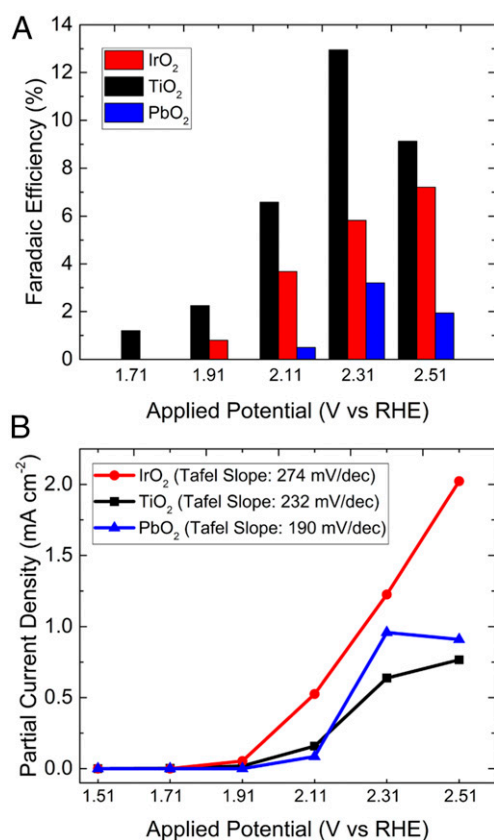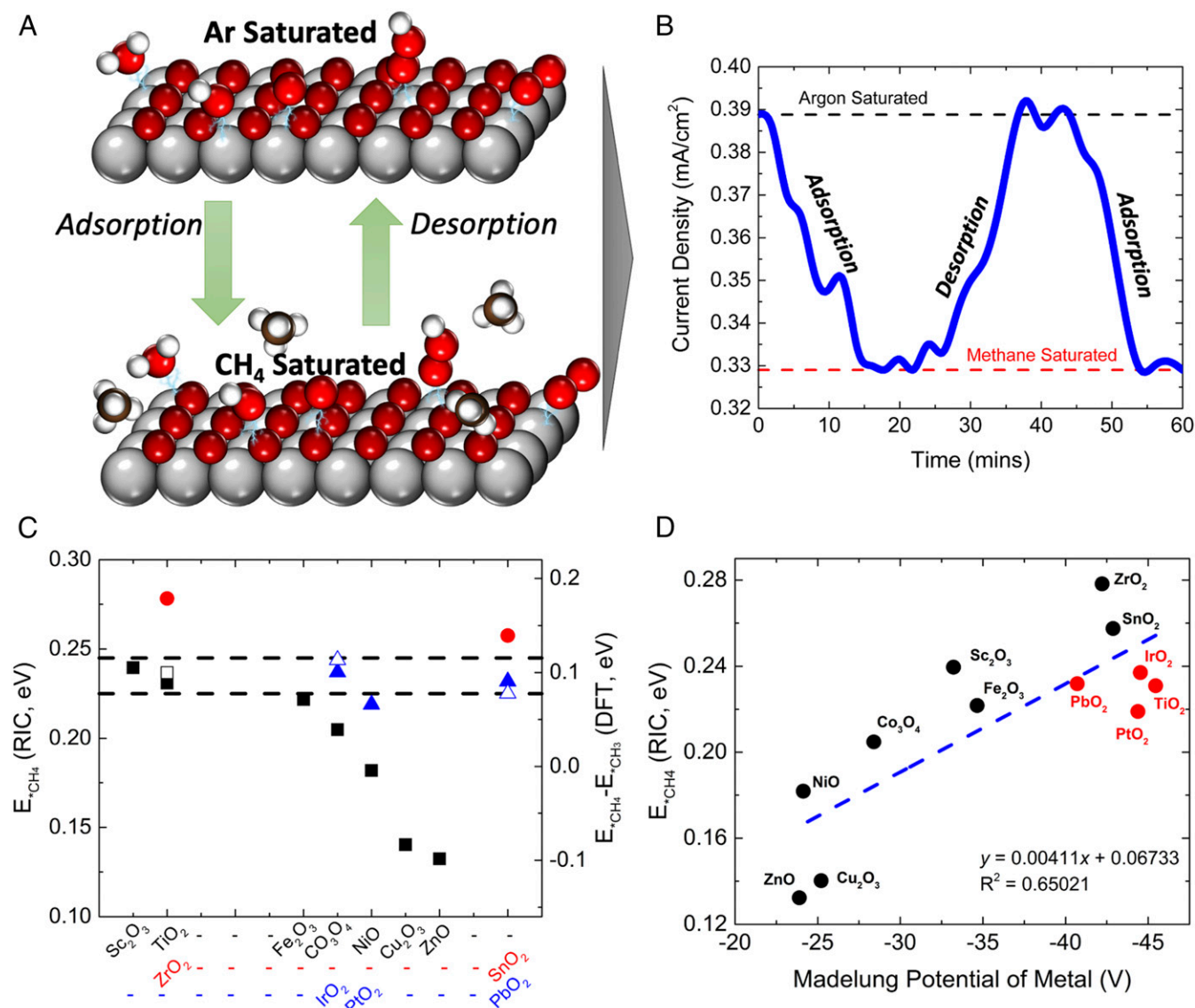
Fig. 3. (*A*) Schematic representation of OER intermediates on (110) surface of TMOs in Ar-saturated and CH$_4$-saturated electrolytes. As the Ar-saturated electrolyte is swapped with CH$_4$-saturated electrolyte, the CH$_4$ adsorbs on the TMO and reduces the number of active sites for OER. Switching the CH$_4$-saturated electrolyte back with Ar-saturated electrolyte allows CH$_4$ desorption and an increase in the number of active sites for OER. Light gray spheres are metal atoms, dark gray spheres are the oxygen atoms from the oxide layer, blue spheres represent oxygen from the electrolyte, red represents carbon, and white represents hydrogen atoms. (*B*) Reversible change in the OER current density with adsorption and desorption of CH$_4$ at a fixed applied potential of 1.52 V versus RHE. (*C*) Estimated binding energies of *CH$_4$ obtained using Everett isotherm for different TMOs at 1.52 V versus RHE. The MOR active TMOs—TiO$_2$, IrO$_2$, PbO$_2$, and PtO$_2$—have similar binding energy in the range 0.22 to 0.25 eV and similar activation energy in the range 0.09 to 0.12 eV. Black squares show the first-row TMOs, red circles show the second-row TMOs, and the blue triangles show the third-row TMOs. (*D*) Scaling relationship between measured binding energy of *CH$_4$ and the Madelung potential of metal in TMOs. The MOR active catalysts—TiO$_2$, IrO$_2$, PbO$_2$, and PtO$_2$—have a higher binding energy of *CH$_4$ and lower Madelung potential.

have higher methane binding (>0.23 eV) energy and lower Madelung potential (< −40 V). All the MOR active catalysts—TiO$_2$, PbO$_2$, IrO$_2$, and PtO$_2$—satisfy this activity criteria. A few outliers here are ZrO$_2$ and SnO$_2$, which satisfy the activity criteria but are not active toward MOR. One of the reasons could be the presence of shared active sites for competitive OER and MOR on ZrO$_2$ and SnO$_2$ (see details in *Competitive Pathways for OER and MOR on TMOs*). Also, the poor electrical conductivity of ZrO$_2$ could be the reason for the lower activity of OER and inactivity of MOR.

Competitive Pathways for OER and MOR on TMOs. The MOR activity descriptors shown in Fig. 3*D* indicate six catalyst candidates that

could be active for MOR, namely, ZrO$_2$, TiO$_2$, IrO$_2$, PbO$_2$, PtO$_2$, and SnO$_2$. Experimental evaluation of 12 TMOs in Fig. 1 shows TiO$_2$, IrO$_2$, PbO$_2$ and PtO$_2$ are the only four active catalysts for MOR. The other two catalysts—SnO$_2$ and ZrO$_2$—are not active for MOR. To further understand the activity and selectivity of MOR on the four candidate catalysts, TiO$_2$, IrO$_2$, PbO$_2$, and SnO$_2$, the OER and MOR pathways and their energy profiles were calculated using DFT. Experimental conditions dictate that these TMO surfaces are oxidized, but there is little information about the nature and distribution of the oxidation states on these catalysts' surfaces. Also, it is well known that the defects on these surfaces can affect reaction pathways (45). Therefore, we evaluate OER pathways on two extreme surface conditions, fully

reduced and fully oxidized states, and then study MOR only on the fully oxidized surface. The following steps for OER were considered, in which * indicates the bare TMO surface:
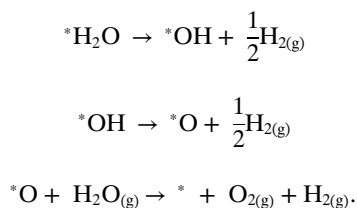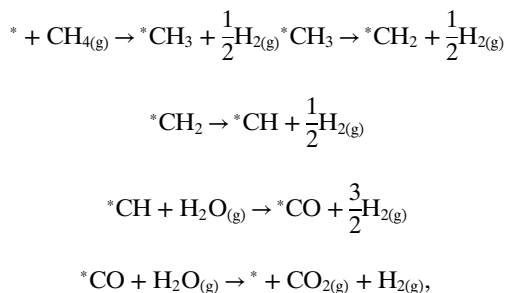
$$^*H_2O \rightarrow {}^*OH + \frac{1}{2}H_{2(g)}$$

$$^*OH \rightarrow {}^*O + \frac{1}{2}H_{2(g)}$$

$$^*O + H_2O_{(g)} \rightarrow {}^* + O_{2(g)} + H_{2(g)}.$$

Fig. 4 A and B show that IrO$_2$ readily catalyzes OER on both the reduced and oxidized surfaces, which agrees well with previous theoretical and experimental findings (59). However, the OER pathways on PbO$_2$, SnO$_2$, and TiO$_2$ surfaces are more complicated and strongly dependent on their oxidation states. The OER pathways on TiO$_2$ and SnO$_2$ proceed preferentially on the reduced surface at the metal center binding site, which suggests that the coordinatively unsaturated metal centers are the active sites for OER. The OER pathway on PbO$_2$ proceeds on the oxidized surface at the bridging oxygen binding site. Also, PbO$_2$ is the only surface on which it is energetically favorable for the bridging oxygen to dissociate from the surface, as seen in *SI Appendix*, Fig. S25. The DFT-predicted OER activity on the sampled surfaces increases in the order PbO$_2$ (bridging O) < SnO$_2$ (on-top M) < TiO$_2$ (on-top M) < IrO$_2$ (on-top M), which aligns very well with the increasing order of experimental current densities for PbO$_2$ (0.2 mA/cm^2), SnO$_2$ (0.3 mA/cm^2), TiO$_2$

(2.5 mA/cm^2), and IrO$_2$ (3.2 mA/cm^2) at 2.1 V versus RHE shown in *SI Appendix*, Fig. S11. This indicates that the chosen computational methods can qualitatively describe the relative activities of these catalytic systems.

To study MOR on these four TMO surfaces, we considered the following steps:

$$^* + CH_{4(g)} \rightarrow {}^*CH_3 + \frac{1}{2}H_{2(g)} \quad {}^*CH_3 \rightarrow {}^*CH_2 + \frac{1}{2}H_{2(g)}$$

$$^*CH_2 \rightarrow {}^*CH + \frac{1}{2}H_{2(g)}$$

$$^*CH + H_2O_{(g)} \rightarrow {}^*CO + \frac{3}{2}H_{2(g)}$$

$$^*CO + H_2O_{(g)} \rightarrow {}^* + CO_{2(g)} + H_{2(g)},$$

where *CH to *CO is a composite step consisting of *CH → *HCOH → *HCO → *CO.

Fig. 4C shows the first step in the catalytic cycle for MOR is comparable in energy to that of OER, which also validates E$_{OH}$–E$_O$ as the common activity descriptors for OER and MOR. The reaction steps here show MOR occurring on a metal center that is occupied by an oxygen atom (M–O, see *SI Appendix*, Table S2). This binding site for catalytic mechanisms has been discussed in zeolites and metal–organic frameworks, but to the best of our knowledge, this mechanism has had little discussion in metal oxides (30). *SI Appendix*, Figs. S15–S17 show the MOR
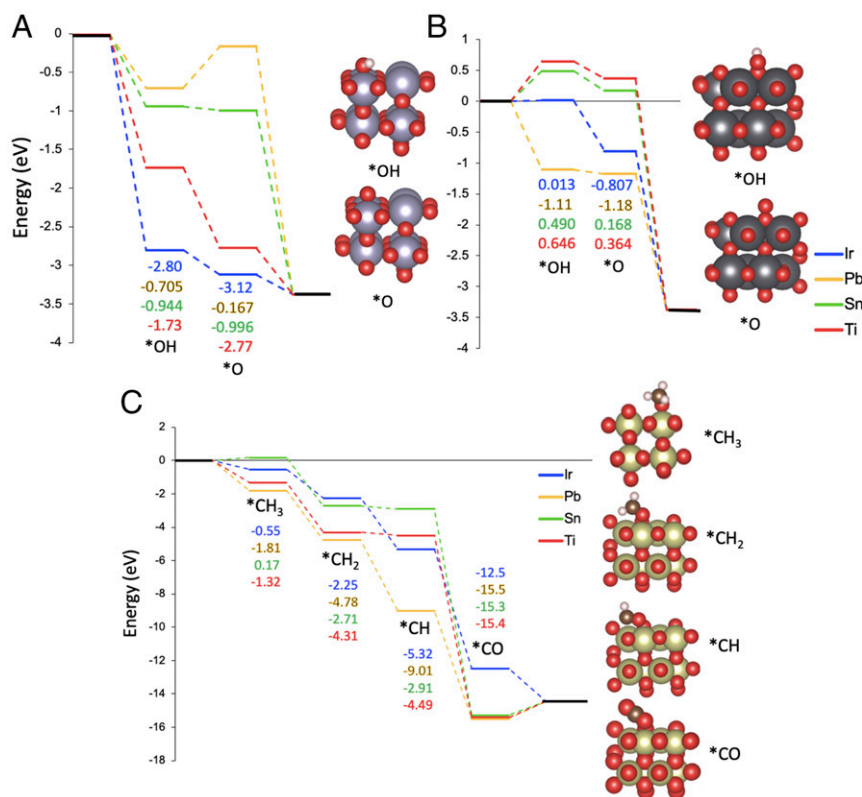
Fig. 4. (*A*) Reaction profile for OER at the metal with oxygen binding site for the fully reduced surface (*B*) Reaction profile for OER at the bridging oxygen binding site for the fully oxidized surface. The relative energies of reaction are shown as a function of reaction coordinate, labeled by *X, where X indicates the adsorbed intermediate. To the right of the plot are pictorial representations of the adsorbed intermediate. Colors denote Sn (silver), Pb (gray), O (red), and H (pink). (*C*) Reaction profile for MOR at the metal with oxygen binding site for the fully oxidized surface. The relative energies of the reaction are shown as a function of reaction coordinate, labeled by *X, where X indicates the adsorbed intermediate along with the pictorial representations of the adsorbed intermediate. Colors denote Ir (gold), O (red), C (brown), and H (pink). All electronic energies are reported using PBE+D3 at an applied potential of 2.11 V versus RHE.
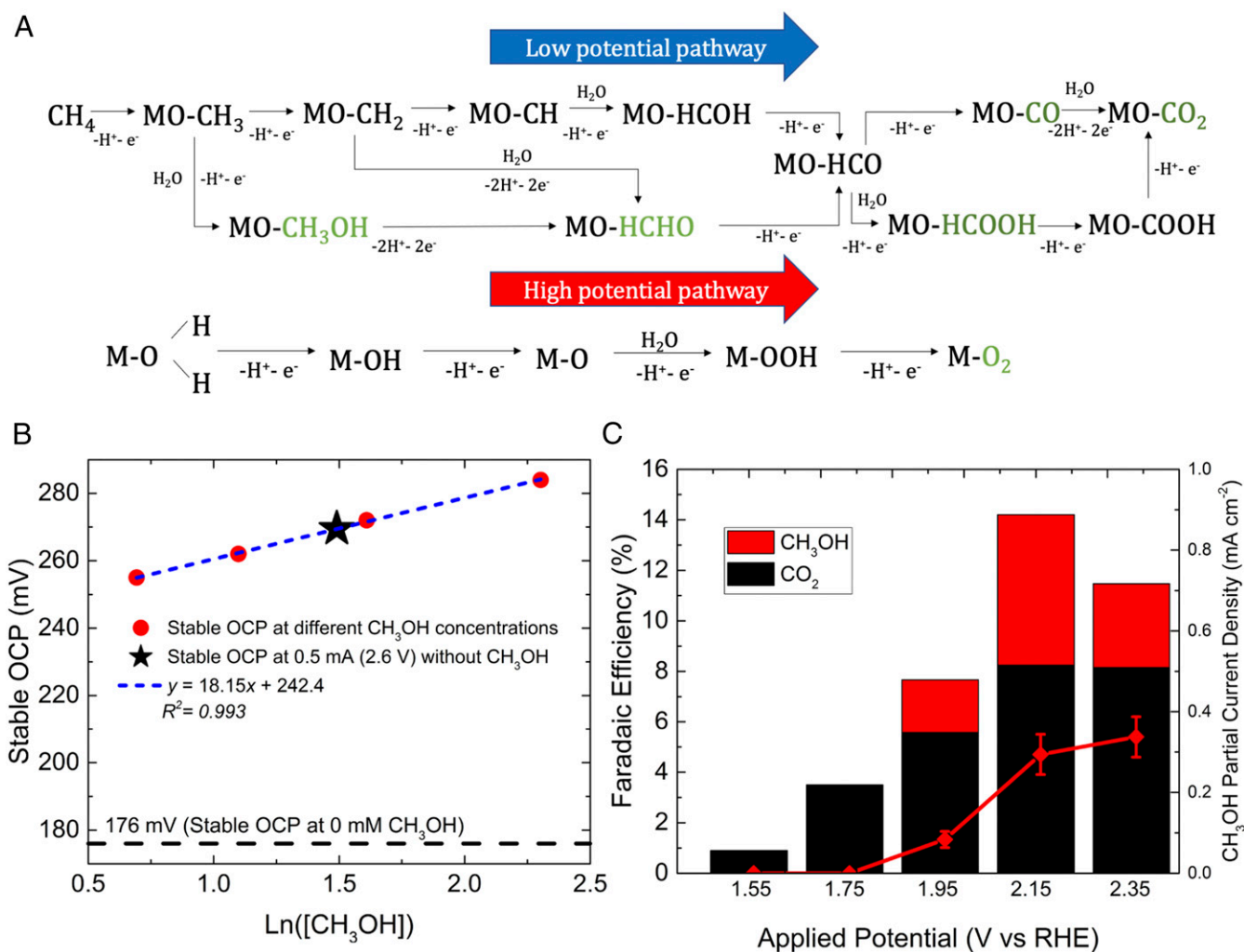
Fig. 5. (*A*) Possible reaction pathways for MOR and OER in an aqueous electrolyte where M represents TMO. The species in green are the possible MOR products. (*B*) The shift in the stable OCP with increasing concentrations of CH_3OH in phosphate buffer electrolyte for an initial current of 0.25 mA at 1.8 V. The linear relation is similar to the Nernst equation. The increase in stable OCP from 176 mV for 0.25 mA to 269 mV for 0.5 mA of initial current in CH_4-saturated phosphate buffer electrolyte without added CH_3OH indicates the formation of *CH_3OH on TiO_2. (*C*) FE and partial current density of CH_3OH on Cu_2O_3–TiO_2 bimetallic catalyst in CH_4-saturated, 0.1 M potassium phosphate buffer.

pathways on alternative binding sites. The first step for MOR in Fig. 4*C* is slightly higher in energy as compared to OER in Fig. 4 *A* and *B*, which is aligned with the experimental observation of lower FEs of MOR on these TMOs. Based on the energies of the reaction pathways on different types of binding sites on TMOs, the M–O binding site is where MOR occurs favorably for all experimentally active systems. M–O is also a recognized intermediate for the OER catalytic cycle; therefore, this binding site is readily available for catalysis on these surfaces. However, the coverage of the M–O site can vary on these catalysts, as the formation of the M–O site is more favorable thermodynamically on TiO_2 and IrO_2 as compared to SnO_2 and PbO_2 (Fig. 4*A*). Although the MOR is more energetically downhill on PbO_2 as seen in Fig. 4*C*, the lower coverage of M–O sites on this catalyst is a reason for its lower MOR activity as compared to TiO_2 (Fig. 2). The reaction steps also indicate that MOR proceeds readily on TiO_2, PbO_2, and IrO_2 but not SnO_2, as the first step in the catalytic cycle is positive for this surface. These DFT results justify the observed MOR activity on TiO_2, PbO_2, and IrO_2 catalysts. To gain a further understanding of the reaction kinetics, the reaction barriers need to be calculated, which is planned for future studies.

Identification of *CH_3OH Intermediate of MOR and Strategy to Harvest CH_3OH. The reaction pathway for MOR proceeds primarily through *CH_x (x = 1, 2, 3, and 4) intermediates at lower potentials, as shown in Fig. 4*C*. However, a few reports have indicated the possibility of forming oxygenated intermediates such as *CH_3OH, *$HCHO$, and *$HCOOH$ during MOR on TMOs (40, 60, 61). Fig. 5*A* shows alternate pathways for MOR going through oxygenated intermediates starting from *CH_3OH → *$HCHO$ → *$HCOOH$ → *CO_2 and a pathway for OER in an aqueous electrolyte on TMOs. The identification of oxygenated intermediates using spectroscopic methods can be very challenging at higher applied potential and current density (62, 63). An alternate method to identify reaction intermediate is by direct measurement of the OCP. OCP is similar to the Nernst potential for a single redox reaction, in which the variation in the local concentration of reactants and products has a direct effect on the OCP value. The stable OCP values were measured on TiO_2 for the initial current of 0.25 mA (1.8 V) with increasing concentrations of CH_3OH—0, 2, 3, 5, and 10 mM—added to CH_4-saturated phosphate buffer electrolyte. Fig. 5*B* shows the increase in stable OCP with increasing the logarithm of CH_3OH concentration, which is similar to the Nernst relation. The

Prajapati et al.
Fundamental insight into electrochemical oxidation of methane towards methanol on transition metal oxides

PNAS | 7 of 9
https://doi.org/10.1073/pnas.2023233118

ENGINEERING

corresponding t-OCP values for different concentrations of CH_3OH are shown in the *SI Appendix*. Fig. 5*B* is used as a calibration curve to relate the change in the OCP of TiO_2 to the formation of $*CH_3OH$. The t-OCP is then measured on TiO_2 for initial currents of 0.25 mA (1.8 V) and 0.5 mA (2.6 V) in CH_4-saturated electrolyte (with no added CH_3OH). The increase in stable OCP values from 176 mV for 0.25 mA to 269 mV for 0.5 mA suggests an increase in $*CH_3OH$ formation, as the concentrations of other species—CH_4, H^+, OH^-, H_2O, and O_2—are constant. Although $*CH_3OH$ was identified on TiO_2, the concentration of free CH_3OH in the electrolyte was below the measurement limit that can be due to the over-oxidation of $*CH_3OH$ to $*HCHO$, $*HCOOH$, and $*CO_2$. *SI Appendix*, Fig. S13 also confirms CH_3OH oxidizes on TiO_2 at potentials >1.9 V versus RHE. To further confirm the formation of these oxygenated intermediates, similar t-OCP measurements were conducted on TiO_2 using varying concentration of HCOOH (*SI Appendix*, section S.11). The stable OCP increased with the increase in the logarithm of HCOOH concentration, similar to the Nernst relation. This indicates both $*CH_3OH$ and $*HCOOH$ could be present on TiO_2 at higher applied potentials. Hence, it is likely that MOR proceeds through two different mechanisms that are potential dependent. At lower applied potentials, MOR progresses through sequential CH_x dissociation, while at higher potentials, MOR proceeds through the formation of $*CH_3OH$, and in both cases, CO_2 is the major MOR product formed over TiO_2.

Under a positive bias >1.4 V, TiO_2 could overcome the barrier for $*CH_4$ dissociation to yield lower fragments of $*CH_x$ of higher binding energy (39), such that the TMO surface is mostly populated with $*CH_3$, leading toward the formation of CO_2. To produce CH_3OH, the $*CH_3$-populated TMOs must be brought in contact with another metal that can provide $*OH$ and prevent overoxidation of CH_3OH. Lin et al. showed that the energy barrier for the reaction of $*CH_3$ with $*OH$ is lowest for Cu—0.17 eV—among other transition metals (64). Cu not only has a lower barrier for CH_3OH formation (64) but also is resistant to further oxidation of CH_3OH (*SI Appendix*, Fig. S13). Fig. 5*C* shows the FE and partial current density of CH_3OH on Cu_2O_3–TiO_2 bimetallic TMOs. The maximum FE of 6% and current density of 0.35 mA/cm² are obtained for CH_3OH on Cu–Ti bimetallic TMOs.

Conclusions and Perspectives

In this article, we develop a fundamental understanding of electrochemical CH_4 oxidation on TMOs and report the binding energy of CH_4 on TMOs under relevant conditions, activity descriptors of MOR, identification of active sites for MOR, detection of $*CH_3OH$ intermediate and its oxidation product, and strategies to harvest CH_3OH by minimizing its overoxidation.

The electrochemical oxidation of CH_4 on TMOs proceeds with the physical adsorption of CH_4 followed by the activation of C–H bonds forming either CH_x intermediates or oxygenated intermediates to yield products such as CO_2, CO, CH_3OH, or HCHO. The physical adsorption of CH_4 involves the transformation of the tetrahedral (T_d) symmetry of CH_4 to a bond-angle–distorted (D_{2d}) structure with an H–C–H bond angle of ~120°. The physical adsorption is governed by the electrostatic interaction of CH_4 with the metal of TMO. To understand the physical adsorption process on TMOs, the binding energy of CH_4 is measured using pulsed-reactant chronoamperometry on 12 stable TMOs in neutral pH electrolyte. The measured binding energy of CH_4 scales linearly with the electrostatic (or Madelung) potential

of metal in TMOs. We hypothesize that the MOR active catalysts should have higher CH_4 binding energy (>0.23 eV) and lower Madelung potential (<−40 V). Out of 12 TMOs studied here, TiO_2, IrO_2, PbO_2, PtO_2, SnO_2, and ZrO_2 satisfy the MOR activity criteria of higher binding energy and lower Madelung potentials. However, the experimental measurements show only TiO_2, IrO_2, PbO_2, and PtO_2 are the active catalysts for MOR. The inactivity of ZrO_2 and SnO_2 toward MOR is due to the poor electrical conductivity and lower population of MOR active sites, respectively.

The competitive pathways of OER and MOR are studied on the promising MOR catalysts—TiO_2, IrO_2, PbO_2, and SnO_2—using DFT to identify the active sites and the mechanism of the oxidation reactions. While the OER pathway on SnO_2, TiO_2, and IrO_2 is favorable on the undercoordinated metal site, this reaction on PbO_2 occurs on the bridging O site. The DFT-predicted OER activity on the sampled surfaces increases in the order PbO_2 (bridging O) < SnO_2 (on-top M) < TiO_2 (on-top M) < IrO_2 (on-top M), which aligns very well with the increasing order of experimental current densities. The M–O intermediate formed on these TMOs is also the most favorable active site for MOR. The energy profiles of MOR on M–O sites are energetically favorable on these TMOs, except SnO_2, for which the first dehydrogenation step is positive. The lower OER current and hence lower M–O active site coverages on SnO_2, along with the higher energy barrier for MOR, are the reasons for its inactivity toward MOR.

We also postulate that the reaction pathway for MOR proceeds primarily through $*CH_x$ (x = 1, 2, 3, and 4) intermediates at lower potentials and through $*CH_xO_y$ intermediates at higher potentials. Here, we develop a technique of t-OCP measurement to identify key reaction intermediates under operating conditions. The steady-state OCP varies linearly with the logarithm of CH_3OH and HCOOH (oxidation product of CH_3OH) concentration in the electrolyte, which is similar to the Nernst potential. The increase in the stable OCP value from 176 mV for 0.25 mA to 269 mV for 0.5 mA confirms the formation of $*CH_3OH$ and its oxidation products at higher potentials. However, the overoxidation of $*CH_3OH$ prevents the accumulation of CH_3OH in measurable quantity in the electrolyte. To produce CH_3OH, we show the $*CH_3$-populated TiO_2 can be mixed with Cu_2O_3 that can provide $*OH$ and prevent overoxidation of CH_3OH. The preliminary result shows that 10% Cu_2O_3 on TiO_2 can increase the desorption of $*CH_3OH$ and hence its FE to 6%. This work provides strategies that can be implemented to produce liquid fuels from CH_4 using bimetallic TMOs.

1. A. H. B. Mostaghimi, T. A. Al-Attas, M. G. Kibria, S. Siahrostami, A review on electro-catalytic oxidation of methane to oxygenates. *J. Mater. Chem. A* **8**, 15575–15590 (2020).
2. B. G. Lougou *et al.*, Analysis of CO2 utilization into synthesis gas based on solar thermochemical CH4-reforming. *J. Energy Chem.* **28**, 61–72 (2019).
3. J. Jang, K. Shen, C. G. Morales-Guio, Electrochemical direct partial oxidation of methane to methanol. *Joule* **3**, 2589–2593 (2019).
4. G. A. Olah, Beyond oil and gas: The methanol economy. *Angew. Chem. Int. Ed. Engl.* **44**, 2636–2639 (2005).

5. M. Ravi, M. Ranocchiari, J. A. van Bokhoven, The direct catalytic oxidation of methane to methanol—A critical assessment. *Angew. Chem. Int. Ed. Engl.* **56**, 16464–16483 (2017).

6. D. Go *et al.*, Atomic layer deposited YSZ overlayer on Ru for direct methane utilization in solid oxide fuel cell. *Ceram. Int.* **46**, 1705–1710 (2020).

7. G. S. Prakash *et al.*, High efficiency direct methanol fuel cell based on poly (styrenesulfonic) acid (PSSA)–poly (vinylidene fluoride) (PVDF) composite membranes. *J. Fluor. Chem.* **125**, 1217–1230 (2004).

8. P. Schwach, X. Pan, X. Bao, Direct conversion of methane to value-added chemicals over heterogeneous catalysts: Challenges and prospects. *Chem. Rev.* **117**, 8497–8520 (2017).

9. A. J. Thakkar, T. Wu, How well do static electronic dipole polarizabilities from gas-phase experiments compare with density functional and MP2 computations? *J. Chem. Phys.* **143**, 144302 (2015).

10. S. Yamamoto, J. B. Alcauskas, T. E. Crozier, Solubility of methane in distilled water and seawater. *J. Chem. Eng. Data* **21**, 78–80 (1976).

11. J. Baltrusaitis, I. Jansen, J. S. Christus, Renewable energy based catalytic CH4 conversion to fuels. *Catal. Sci. Technol.* **4**, 2397–2411 (2014).

12. N. Spinner, W. E. Mustain, Electrochemical methane activation and conversion to oxygenates at room temperature. *J. Electrochem. Soc.* **160**, F1275–F1281 (2013).

13. J. C. Fornaciari *et al.*, A perspective on the electrochemical oxidation of methane to methanol in membrane electrode assemblies. *ACS Energy Lett.* **5**, 2954–2963 (2020).

14. E. P. Murray, T. Tsai, S. A. Barnett, A direct-methane fuel cell with a ceria-based anode. *Nature* **400**, 649–651 (1999).

15. J. B. Wang, J.-C. Jang, T.-J. Huang, Study of Ni-samaria-doped ceria anode for direct oxidation of methane in solid oxide fuel cells. *J. Power Sources* **122**, 122–131 (2003).

16. Z. Zhan, Y. Lin, M. Pillai, I. Kim, S. A. Barnett, High-rate electrochemical partial oxidation of methane in solid oxide fuel cells. *J. Power Sources* **161**, 460–465 (2006).

17. J. Liu, S. A. Barnett, Operation of anode-supported solid oxide fuel cells on methane and natural gas. *Solid State Ion.* **158**, 11–16 (2003).

18. C. Liu, J. Ye, J. Jiang, Y. Pan, Progresses in the preparation of coke resistant Ni-based catalyst for steam and CO2 reforming of methane. *ChemCatChem* **3**, 529–541 (2011).

19. A. Ideris, E. Croiset, M. Pritzker, A. Amin, Direct-methane solid oxide fuel cell (SOFC) with Ni-SDC anode-supported cell. *Int. J. Hydrogen Energy* **42**, 23118–23129 (2017).

20. E. S. Putna, J. Stubenrauch, J. M. Vohs, R. J. Gorte, Ceria-based anodes for the direct oxidation of methane in solid oxide fuel cells. *Langmuir* **11**, 4832–4837 (1995).

21. B. C. H. Steele, I. Kelly, H. Middleton, R. Rudkin, Oxidation of methane in solid state electrochemical reactors. *Solid State Ion.* **28**, 1547–1552 (1988).

22. H. Kim, C. Lu, W. L. Worrell, J. M. Vohs, R. J. Gorte, Cu-Ni cermet anodes for direct oxidation of methane in solid-oxide fuel cells. *J. Electrochem. Soc.* **149**, A247–A250 (2002).

23. H. Ding, Z. Tao, S. Liu, Y. Yang, A redox-stable direct-methane solid oxide fuel cell (SOFC) with Sr2FeNb0. 2Mo0. 8O6− δ double perovskite as anode material. *J. Power Sources* **327**, 573–579 (2016).

24. R. L. Cook, A. F. Sammells, Ambient temperature methane activation to condensed species under cathodic conditions. *J. Electrochem. Soc.* **137**, 2007–2008 (1990).

25. T. Otagawa, S. Zaromb, J. R. Stetter, Electrochemical oxidation of methane in non-aqueous electrolytes at room temperature: Application to gas sensors. *J. Electrochem. Soc.* **132**, 2951–2957 (1985).

26. M. Stoukides, Electrochemical studies of methane activation. *J. Appl. Electrochem.* **25**, 899–912 (1995).

27. J. Cassidy, S. B. Khoo, S. Pons, M. Fleischmann, Electrochemistry at very high potentials: The use of ultramicroelectrodes in the anodic oxidation of short-chain alkanes. *J. Phys. Chem.* **89**, 3933–3935 (1985).

28. K. W. Frese Jr, Partial electrochemical oxidation of methane under mild conditions. *Langmuir* **7**, 13–15 (1991).

29. F. Hahn, C. A. Melendres, Anodic oxidation of methane at noble metal electrodes: An 'in situ' surface enhanced infrared spectroelectrochemical study. *Electrochim. Acta* **46**, 3525–3534 (2001).

30. Á. Szécsényi, G. Li, J. Gascon, E. A. Pidko, Mechanistic complexity of methane oxidation with H2O2 by single-site Fe/ZSM-5 catalyst. *ACS Catal.* **8**, 7961–7972 (2018).

31. M.-S. Liao, Q.-E. Zhang, Dissociation of methane on different transition metals. *J. Mol. Catal. Chem.* **136**, 185–194 (1998).

32. G. Psofogiannakis, A. St-Amant, M. Ternan, Methane oxidation mechanism on Pt(111): A cluster model DFT study. *J. Phys. Chem. B* **110**, 24593–24605 (2006).

33. Y. Chen, D. G. Vlachos, Density functional theory study of methane oxidation and reforming on Pt (111) and Pt (211). *Ind. Eng. Chem. Res.* **51**, 12244–12252 (2012).

34. D. Schröder, H. Schwarz, FeO⊕ activates methane. *Angew. Chem. Int. Ed. Engl.* **29**, 1433–1434 (1990).

35. A. Dong *et al.*, Single PdO loaded on boron nanosheet for methane oxidation: A DFT study. *Prog. Nat. Sci.* **29**, 367–369 (2019).

36. Z.-J. Zhao, A. Kulkarni, L. Vilella, J. K. Nørskov, F. Studt, Theoretical insights into the selective oxidation of methane to methanol in copper-exchanged mordenite. *ACS Catal.* **6**, 3760–3766 (2016).

37. G. Fu, Z.-N. Chen, X. Xu, H.-L. Wan, Understanding the reactivity of the tetrahedrally coordinated high-valence d0 transition metal oxides toward the C-H bond activation of alkanes: A cluster model study. *J. Phys. Chem. A* **112**, 717–721 (2008).

38. A. A. Latimer *et al.*, Understanding trends in C-H bond activation in heterogeneous catalysis. *Nat. Mater.* **16**, 225–229 (2017).

39. F. Abild-Pedersen *et al.*, Scaling properties of adsorption energies for hydrogen-containing molecules on transition-metal surfaces. *Phys. Rev. Lett.* **99**, 016105 (2007).

40. L. Arnarson *et al.*, Fundamental limitation of electrocatalytic methane conversion to methanol. *Phys. Chem. Chem. Phys.* **20**, 11152–11159 (2018).

41. O. B. Shmychkova, V. A. Knysh, T. V. Luk'yanenko, R. Amadelli, A. B. Velichenko, Electrocatalytic processes on PbO 2 electrodes at high anodic potentials. *Surg. Eng. Appl. Electrochem.* **54**, 38–46 (2018).

42. G. Kresse, J. Furthmüller, Efficiency of ab-initio total energy calculations for metals and semiconductors using a plane-wave basis set. *Comput. Mater. Sci.* **6**, 15–50 (1996).

43. S. Grimme, J. Antony, S. Ehrlich, H. Krieg, A consistent and accurate ab initio parametrization of density functional dispersion correction (DFT-D) for the 94 elements H-Pu. *J. Chem. Phys.* **132**, 154104 (2010).

44. J. P. Perdew, K. Burke, M. Ernzerhof, Generalized gradient approximation made simple. *Phys. Rev. Lett.* **77**, 3865–3868 (1996).

45. J. K. Nørskov *et al.*, Origin of the overpotential for oxygen reduction at a fuel-cell cathode. *J. Phys. Chem. B* **108**, 17886–17892 (2004).

46. K. Mathew, R. Sundararaman, K. Letchworth-Weaver, T. A. Arias, R. G. Hennig, Implicit solvation model for density-functional study of nanocrystal surfaces and reaction pathways. *J. Chem. Phys.* **140**, 084106 (2014).

47. Y. Tsuji, K. Yoshizawa, Adsorption and activation of methane on the (110) surface of rutile-type metal dioxides. *J. Phys. Chem. C* **122**, 15359–15381 (2018).

48. J. Oscik, A. Dabrowski, M. Jaroniec, W. Rudzinski, Effects of surface heterogeneity in adsorption from binary liquid mixtures. I. Adsorption from ideal solutions. *J. Colloid Interface Sci.* **56**, 403–411 (1976).

49. F. C. Nart, T. Iwasita, M. Weber, In situ FTIR study on the adsorption of phosphate species on well ordered platinum (111) single crystal surfaces. *Ber. Bunsenges. Phys. Chem* **97**, 737–738 (1993).

50. R. Gisbert, G. García, M. T. M. Koper, Adsorption of phosphate species on poly-oriented Pt and Pt (1 1 1) electrodes over a wide range of pH. *Electrochim. Acta* **55**, 7961–7968 (2010).

51. S. Cherevko *et al.*, Oxygen and hydrogen evolution reactions on Ru, RuO2, Ir, and IrO2 thin film electrodes in acidic and alkaline electrolytes: A comparative study on activity and stability. *Catal. Today* **262**, 170–180 (2016).

52. K. Yoshizawa, Two-step concerted mechanism for alkane hydroxylation on the ferryl active site of methane monooxygenase. *J. Biol. Inorg. Chem.* **3**, 318–324 (1998).

53. K. Yoshizawa, T. Ohta, T. Yamabe, R. Hoffmann, Dioxygen cleavage and methane activation on diiron enzyme models: A theoretical study. *J. Am. Chem. Soc.* **119**, 12311–12321 (1997).

54. A. F. Shestakov, A. E. Shilov, Five-coordinate carbon hydroxylation mechanism. *J. Mol. Catal. Chem.* **105**, 1–7 (1996).

55. K. Yoshizawa, T. Yamabe, R. Hoffmann, Possible intermediates for the conversion of methane to methanol on dinuclear iron centers of methane monooxygenase models. *New J. Chem.* **21**, 151–161 (1997).

56. P. E. M. Siegbahn, Trends of metal-carbon bond strengths in transition metal complexes. *J. Phys. Chem.* **99**, 12723–12729 (1995).

57. J. A. M. Simoes, J. L. Beauchamp, Transition metal-hydrogen and metal-carbon bond strengths: The keys to catalysis. *Chem. Rev.* **90**, 629–688 (1990).

58. A. Walsh, K. T. Butler, Prediction of electron energies in metal oxides. *Acc. Chem. Res.* **47**, 364–372 (2014).

59. Y. Ping, R. J. Nielsen, W. A. Goddard 3rd, The reaction mechanism with free energy barriers at constant potentials for the oxygen evolution reaction at the IrO2 (110) surface. *J. Am. Chem. Soc.* **139**, 149–155 (2017).

60. N. Spinner, W. E. Mustain, Electrochemical methane activation and conversion to oxygenates at room temperature. *ECS Trans.* **53**, 1–20 (2013).

61. M. Ma *et al.*, Ultrahigh electrocatalytic conversion of methane at room temperature. *Adv. Sci. (Weinh.)* **4**, 1700379 (2017).

62. F. Jiao, B. Hasa, B. H. Ko, B. Xu, Flow electrolyzer mass spectrometry with a gas diffusion electrode design. *Angew. Chem.* **60**, 3277–3282 (2020).

63. M. Dunwell *et al.*, The central role of bicarbonate in the electrochemical reduction of carbon dioxide on gold. *J. Am. Chem. Soc.* **139**, 3774–3783 (2017).

64. Y.-Z. Lin *et al.*, Energetics of chemisorption and conversion of methane on transition metal surfaces. *J. Mol. Struct. THEOCHEM* **587**, 63–71 (2002).

Prajapati et al.
Fundamental insight into electrochemical oxidation of methane towards methanol on transition metal oxides

PNAS | 9 of 9
https://doi.org/10.1073/pnas.2023233118

ENGINEERING

www.manaraa.com